Polarization-independent Spatial Kramers-Kronig medium for omnidirectional reflectionless absorption of unpolarized light

Check for updates

Quanping Li[1], Yu Luo [2] ✉, Jingjing Zhang [3,4] ✉, Yuan Gao[1], Jingxin Tang[1], Xiaojun Hu[1] & Dexin Ye [1] ✉

Spatial Kramers-Kronig (KK) media offer a possible route to obtain omnidirectional light absorption within a thin layer of material. However, the experimental realizations are typically limited to a specific polarization, i.e., either transverse electric (TE) or transverse magnetic (TM), hence lacking specific implementations for the absorption of unpolarized light. In this work, we propose theoretically and demonstrate experimentally a polarization-independent KK medium which performs omnidirectional reflectionless absorption for both TE and TM polarized waves. Our design makes use of a special matryoshka metamaterial, whose electric and magnetic responses can be independently controlled with minimized crosstalk. To extend the absorption spectrum, the inner truncation boundary of the KK medium is set at a position far away from the spatial Lorentz resonance, where the constitutive parameter of the metamaterial remains unitary over a broad frequency band. A mini anechoic chamber, 6.83-wavelength in diameter, is constructed using the designed annulus-shaped KK medium. The measured fields for both TE and TM polarizations confirm the polarization-independent omnidirectional and nearly reflectionless absorption in a broadband frequency range.

The absorption of electromagnetic energies is of great importance in a wide range of applications[1–4], including electromagnetic compatibility[5,6], radar cross-section reduction and energy harvesting[7–9], etc. Traditional pyramidal and multilayer dielectric absorbers are broadly used in microwave engineering for scattering and radiation measurements[10]. However, due to their poor performance at large impinging angles and electrically large size, these absorbers usually require the conventional anechoic chambers to be adequately large, e.g., tens to several thousands of wavelengths[10–13]. Metamaterials offer the prospect of implementing compact absorbers with ultrasubwavelength thicknesses. Since the advent of the first metamaterial absorber (MMA) in 2008[14], the design and implementation of MMAs have been a hot topic till date[1,15–20]. However, in most previous works, high absorption efficiencies can only be obtained at a single or several specific illumination angles[21,22]. The realization of omnidirectional absorption with high efficiency has been widely acknowledged as a challenging task due to the intrinsic angular selective impedance match[23]. Although the well-known uniaxial perfectly matched layer (UPML), previously defined mathematically in computational electromagnetics[24,25], have been theoretically demonstrated to allow omnidirectional absorption, the requirements on

gain elements render them difficult to implement practically. To the best of our knowledge, the experimentally implemented UPML absorbers are all with reduced parameters[23,26], and thus can optimally work only with specific incident angles. Similarly, the absorptive parity-time symmetric metamaterials[27–29] and transformation optical media[30,31] face the same challenge owing to the requirements on gain elements.

In 2015, Horsley et al. theoretically demonstrated that a class of isotropic, one-dimensionally (1D) inhomogeneous susceptibility profiles can be utilized to realize omnidirectionally perfect absorption without involving any gain elements, provided that they satisfy the spatial Kramers-Kronig (KK) relation[32–37]. Recently, it has been shown that, apart from achieving polarization-independent broadband omnidirectional and direction-dependent invisibility[38], the spatial KK relation can also be extended to X-ray nanoimaging and chiral phase modulation[39,40], showing great promises for all-optical functional devices in quantum information processing and optical communication networks. So far, the spatial KK media for the absorption of TE-polarized waves have been demonstrated experimentally by designing gradient mesoscopic structures with specially tailored electric responses[41–43]. To the best of

[1]Laboratory of Applied Research on Electromagnetics, Zhejiang University, Hangzhou 310027, China. [2]National Key Laboratory of Microwave Photonics, Nanjing University of Aeronautics and Astronautics, Nanjing 211106, China. [3]Institute of Electromagnetic Space, Southeast University, Nanjing 210096, China. [4]State Key Laboratory of Millimeter Waves, Southeast University, Nanjing 210096, China. ✉e-mail: yu.luo@nuaa.edu.cn; zhangjingjing@seu.edu.cn; desy@zju.edu.cn

our knowledge, simultaneous perfect absorption for both TE and TM polarizations has yet to be realized experimentally, probably owing to the difficulty in implementing isotropic spatial KK profiles in practice.

In this work, we report the experimental realization of a polarization-independent omnidirectionally impedance-matched absorber utilizing the spatial KK medium. To realize the required electric and magnetic responses simultaneously, we propose a matryoshka metamaterial, whose effective permittivity and permeability can be independently tuned to the spatial KK profile with minimized crosstalk. To extend the absorption bandwidth, the inner truncation boundary is set at a position far away from the spatial Lorentz resonance. As a result, the metamaterial at the truncation boundary has constant permittivity and permeability over a broadband frequency range. To demonstrate the polarization-independent omnidirectional absorption performance, a cylindrical anechoic chamber, 6.83-wavelength in diameter, is fabricated and implemented with the designed annulus-shaped spatial KK absorber. Analytical solutions, full-wave simulations, and experimental measurements all confirm the polarization-independent omnidirectional reflectionless absorption feature. Our design strategy can be easily extended to higher frequencies, paving a way to implement polarization-independent absorbers for applications in photovoltaics, bolometry, photodetection, stealth technology, mechanical manipulation, etc.[44–46].

Results and discussion
Theoretical analysis

Previous literature shows that a spatial KK profile can be achieved utilizing a spatially inhomogeneous dispersive metamaterial, whose relative permittivity ε_r (or permeability μ_r) is characterized by an r-dependent Lorentz resonance, in the form of[43,47]

$$\varepsilon_r(\omega, r) = 1 - \frac{\omega_P^2}{\omega^2 + i\gamma\omega - (\omega_L - qr)^2}. \quad (1)$$

Here, $\omega_L{-}qr$, γ, and ω_P are the resonance, damping, and plasma frequencies, respectively. q determines the gradient of this r-dependent resonance frequency. Such a spatially inhomogeneous profile spans over the whole space (from $r = 0$ to $r = +\infty$), and thus has to be truncated for the practical implementation. We highlight that an infinite spatial KK medium can achieve perfect light absorption at any frequency, whereas the truncated one can only absorb light over a finite spectrum. Hence, the truncation boundaries must be properly designed to cover the frequency range of interest. There are in general two criteria: (1) at the inner truncation boundary, $\varepsilon_r(\omega, r) \rightarrow 1$ (i.e., the KK medium is impedance matched to air) over the whole frequency range of interest; (2) at the outer truncation boundary, $\omega_L{-}qr < 0$ such that light propagating from the inner to the outer truncation boundary can experience the spatial Lorentz resonance to get absorbed without any reflection. These criteria require the two truncation boundaries to be set far away from the spatial Lorentz resonance.

To give a quantitative illustration, we consider a spatial Lorentz-profile medium with $\omega_P = 0.4\omega_0$, $\omega_L = 2.35\omega_0$, $\gamma = 0.02\omega_0$, and $q = 0.1\omega_0/\lambda_0$ (λ_0 is the wavelength in vacuum for frequency ω_0). Figure 1a plots the real and imaginary parts of $\varepsilon_r(\omega, r)$ as a function of ω and r. To give more details, Fig. 1b plots the $\varepsilon_r(\omega, r)$ as a function of r at three different frequencies, $\omega = 0.9\omega_0$, $\omega = 1.0\omega_0$ and $\omega = 1.1\omega_0$, respectively. Note that when the inner truncation boundary is set at $r = 10\lambda_0$, the permittivities at
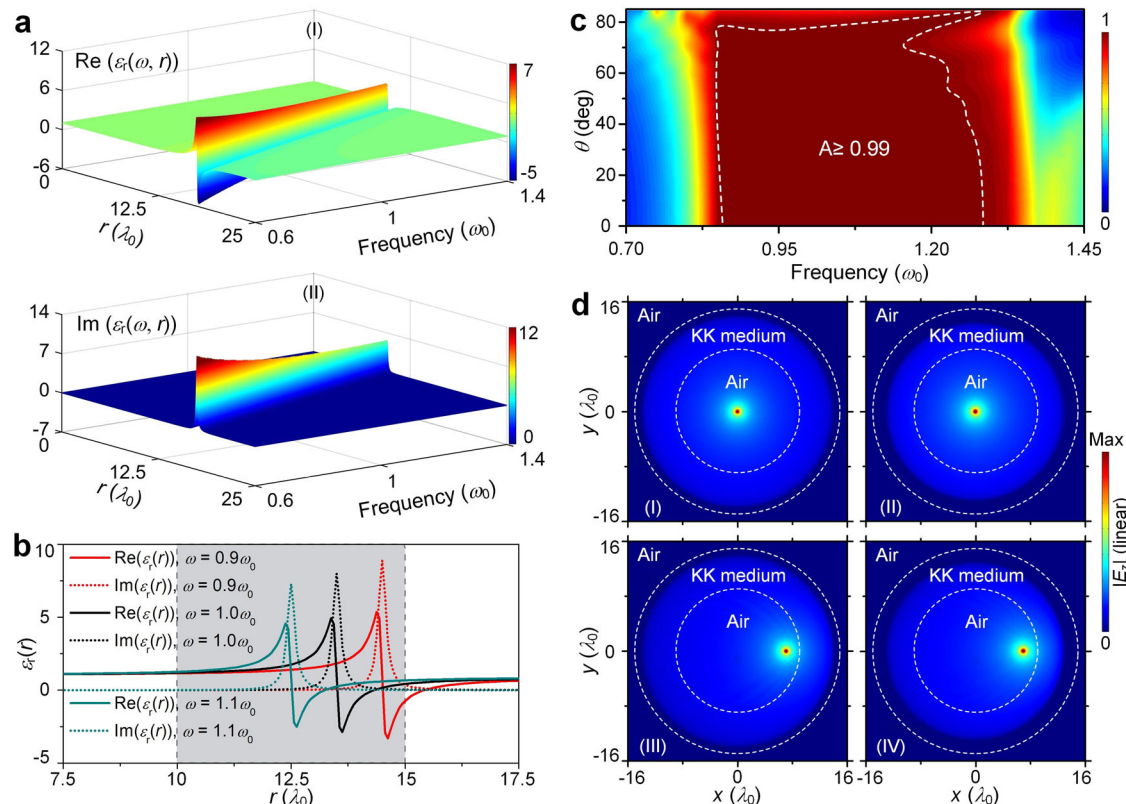

Fig. 1 | Space-frequency KK permittivity profile. a Real (I) and imaginary (II) parts of the permittivity profile defined by Eq. (1), with $\omega_P = 0.4\omega_0$, $\omega_L = 2.35\omega_0$, $\gamma = 0.02\omega_0$, and $q = 0.1\omega_0/\lambda_0$. **b** The r-dependent spatial permittivity profile at $\omega = 0.9\omega_0$, $\omega = 1.0\omega_0$ and $\omega = 1.1\omega_0$. **c** Calculated absorptance A as functions of the incident angle and working frequency for the air-matched KK medium slab.

d Simulated amplitude distributions while placing a line source with a z-polarized electric field in the air region surrounded by the cylindrical air-matched KK medium. Panels I, III show the electric field amplitude distributions at $\omega = 0.95\omega_0$ when the source is located at $(0, 0)$ and $(7\lambda_0, 0)$, respectively. Panels II, IV show the corresponding results at $\omega = 1.05\omega_0$.
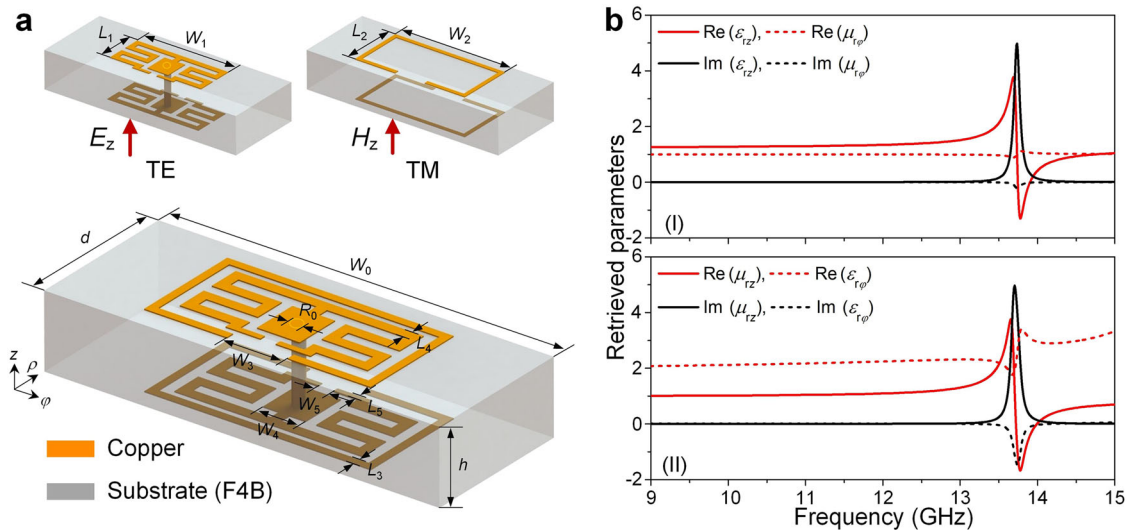
Fig. 2 | Design of the unit for the polarization-independent KK profile.
a Geometry of the matryoshka structure composed of metallic split rings and deformed I-shaped metallic patterns. **b** Retrieved complex constitutive parameters along different directions, with $d = 2.5$ mm, $W_0 = 6.5$ mm, $W_1 = 2$ mm,

$W_2 = 2.47$ mm, $W_3 = 1$ mm, $W_4 = 0.7$ mm, $W_5 = 0.25$ mm, $L_1 = 1.225$ mm, $L_2 = 1.82$ mm, $L_3 = 0.135$ mm, $L_4 = 0.175$ mm, $L_5 = 0.1$ mm, $R_0 = 0.2$ mm and $h = 1.2$ mm.

$0.9\omega_0$ ($\varepsilon_r = 1.17$), $1.0\omega_0$ ($\varepsilon_r = 1.19$), and $1.1\omega_0$ ($\varepsilon_r = 1.24$) remain a constant around 1.2 with negligible imaginary parts. In other words, setting $r = 10\lambda_0$ can readily minimize the reflection at the inner truncation boundary from $0.9\omega_0$ to $1.1\omega_0$, if the background has a permittivity of 1.2. On the other hand, to ensure the total absorption, the outer truncation boundary is set at $r = 15\lambda_0$, (i.e., the truncated spatial permittivity Lorentz-profile medium has a thickness of $5\lambda_0$). Considering practical applications, it is necessary to make the spatial permittivity Lorentz-profile medium impedance matched to air. To this end, we can introduce a thin layer with the permittivity linearly varying from 1 to 1.2 within $r = 9\lambda_0$ and $r = 10\lambda_0$ ($1\lambda_0$ in thick). This linear-profile medium can be easily obtained in a broad frequency band using dielectric-air composites, according to the Maxwell Garnett mixing principle[48]. It should be noted that this linear-profile medium improves the impedance matching and extends the operating bandwidth, especially for larger incident angles. Detailed discussions on the impact of the linear-profile medium can be found in Supplementary Note 1. In our previous work, such a linear-profile medium is not required, because the proposed spatial KK profile involves two typical Lorentz resonances, whose relative permittivity is equal to 1 at a special position[42]. The inner truncation boundary is set at this position, and the KK medium is then impedance matched to free space. Finally, to show the absorption behavior of the whole KK medium (comprised of $5\lambda_0$-thick spatial Lorentz-profile medium and $1\lambda_0$-thick linear-profile medium), we plot in Fig. 1c absorptance A as functions of the incident angle θ and working frequency ω. The algorithm used in the calculation is the same as our previous work[49]. Apparently, over a broad frequency band from $0.85\omega_0$ to $1.15\omega_0$, the absorptance $A > 99\%$ is obtained when the incident angle varies from $0°$ to $78°$, confirming the broadband nearly omnidirectionally reflectionless absorption.

Such a finite air-matched cylindrical KK medium is an excellent candidate to realize miniaturized anechoic chamber. As an example, we use this air-matched permittivity profile to construct a cylindrical anechoic chamber. To verify its absorption behavior, we perform full-wave simulations by placing a line source with a z-polarized electric field at $(0, 0)$ and $(7\lambda_0, 0)$ within this anechoic chamber. To illustrate the broadband responses, simulations are conducted at two different frequencies $0.95\omega_0$ (panels I, III of Fig. 1d) and $1.05\omega_0$ (panels II, IV of Fig. 1d). The results clearly show that, at both frequencies, light

impinging upon the boundary $r = 9\lambda_0$ smoothly goes into the KK medium without any observable reflection and eventually gets dissipated at the positions of the corresponding spatial Lorentz resonances. To quantitatively evaluate the reflection, we define R_{max}/R_{min} as the maximum standing wave radio. Here, R_{max} and R_{min} are the maximum and minimum field amplitudes normalized to the line source field in free space (note that $R_{max}/R_{min} = 1$ corresponds to zero reflection in the chamber). The calculated R_{max}/R_{min} in panels I, II, III, and IV of Fig. 1d are only 1.01, 1.02, 1.13 and 1.11, respectively, confirming the source-independent absorption behavior of the anechoic chamber designed above.

Design and simulation
Our purpose is to realize a cylindrical spatial KK medium to absorb unpolarized light. It requires both the axial permittivity and permeability profiles to satisfy Eq. (1). In order to design a unit cell with desired magnetic and electric Lorentz resonances with negligible crosstalk, we introduce a matryoshka structure composed of metallic split rings and deformed I-shaped metallic patterns[50–53]. The split rings (top right corner of Fig. 2a) and I-shaped patterns (top left corner of Fig. 2a) are responsible to absorb TM (with a z-polarized magnetic field) and TE (with a z-polarized electric field) polarized waves, respectively. Such unit cells are aligned periodically along the z and azimuthal φ directions. The radial width d is fixed as 2.5 mm for all unit cells. It is smaller than $\lambda_0/10$ at the operating frequencies from 10 to 10.5 GHz. Hence, the reflection resulting from the structural discretization is minimized and the whole structure can be considered as homogeneous[42,43]. To retrieve the effective permittivity and permeability, we perform full-wave simulations on this unit cell using periodic boundary condition. The detailed descriptions about the simulation setup are given in Supplementary Note 2. As a special example, Fig. 2b plots the effective permittivity and permeability of the unit cell using the retrieval algorithm of reference[54]. Interestingly, such a unit cell supports electric and magnetic resonances at the same frequency with negligible crosstalk.

The polarization-independent spatial KK medium requires that the electric and magnetic resonances both have the same r-dependent resonance frequency $\omega_L—qr$. To realize such a response, we line up 30 layers along the radial direction from $r_2 = 61d$ to $r_3 = 90d$, ($d = 2.5$ mm) and gradually increase W_1 from 2.0 mm to 3.07 mm and W_2 from 2.47 mm to
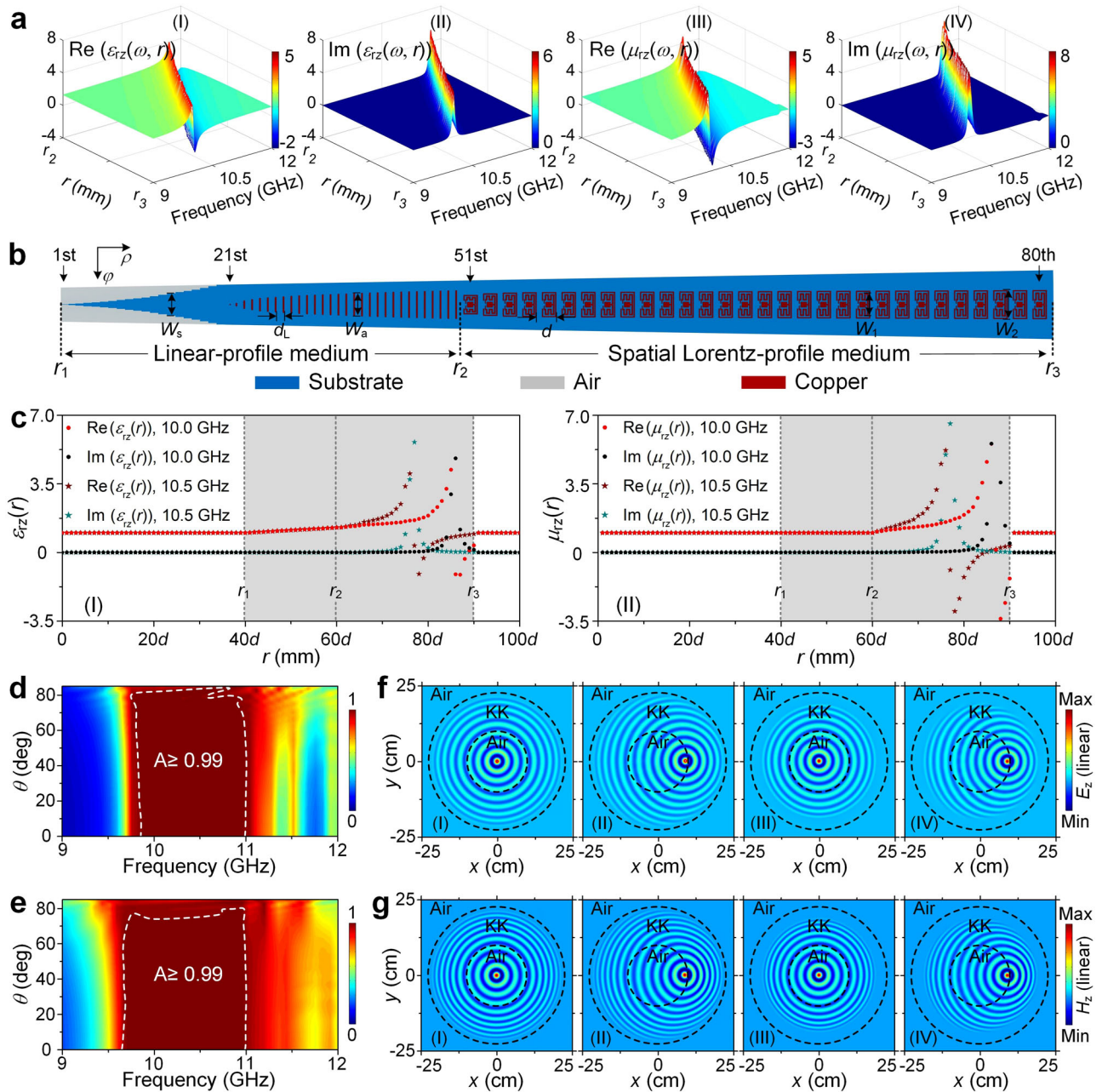
Fig. 3 | Actual design of the polarization-independent spatial KK medium.
a Retrieved axial relative permittivity (I, II) and permeability (III, IV) of the spatial Lorentz-profile medium, dependent on the frequency and the space variable r.
b Entire strip of unit cells along the radial direction to construct the cylindrical air-matched spatial KK medium. In the spatial Lorentz-profile medium ($r_2 \leq r < r_3$), the parameters W_1 and W_2 for each unit (Detailed geometric dimensions they denote can be found in Fig. 2a) change along the radial direction to form the desired spatial profile. Similarly, the parameters W_s and W_a, denoting the lengths of the dielectric strips and metallic wires, respectively, also change along the radial direction to constitute the linear-profile medium ($r_1 \leq r < r_2$) (Details can be found in Supplementary Note 4). d_L and d denote the periods of units to construct the Linear-profile medium and the Lorentz-profile medium along the radial direction, respectively. **c** r-dependent axial permittivity (I) and permeability (II) of the designed cylindrical anechoic chamber using the air-matched KK medium (gray regions) at 10 and 10.5 GHz. **d, e** Calculated absorptance of a slab with the spatial KK profiles shown in (**c**), under TE (**d**), and TM (**e**) wave incidences, respectively. **f** Simulated z-polarized electric field distributions while placing a line source inside the anechoic chamber composed of the designed KK medium. Panels I and II show the results at 10 GHz when the line source is located at (0, 0), and (9 cm, 0), respectively. Panels III and IV show the corresponding results at 10.5 GHz. **g** Simulated magnetic field distributions when the line source is with a z-polarized magnetic field.

3.70 mm (other dimensions remain unchanged). Figure 3a depicts the retrieved axial permittivity and permeability of the designed spatial Lorentz-profile medium dependent on the frequency (ω) and the radius (r). The detailed dimensions of W_1 and W_2 in each layer from r_2 to r_3 are shown in Supplementary Note 3. Through proper numerical fittings, such

space-frequency dependences can be described by,

$$\varepsilon_{rz}(\omega, r) = 1.2 - \frac{(2 \times 10^9)^2}{\omega^2 + i\omega \times 70 \times 10^6 - (14.78 \times 10^9 - 0.055 \times 10^9 \times \frac{r}{d})^2} \tag{2}$$

and

$$\mu_{rz}(\omega, r) = 1 - \frac{(2.1 \times 10^9)^2}{\omega^2 + i\omega \times 60 \times 10^6 - (14.78 \times 10^9 - 0.055 \times 10^9 \times \frac{r}{d})^2},$$

(3)

in accordance with our theoretical analysis above.

At the inner truncation boundary ($r = r_2$) of the spatial Lorentz profiles, the constitutive parameters from 10 GHz to 10.5 GHz are constants: $\varepsilon_{rz} \approx 1.3$, $\varepsilon_{r\varphi} \approx 2.2$, and $\mu_{rz} \approx \mu_{r\varphi} \approx 1$. As analyzed above, a linear-profile medium is introduced to achieve impedance matching with air. In particular, the required linear-profile medium is nonmagnetic but anisotropic. In our implementation, this linear-profile medium is divided into 2 parts: the dielectric-air composite (with ε_{rz} linearly varying from 1 to 1.3 and $\varepsilon_{r\varphi}$ linearly varying from 1 to 1.5), and the cut-wire metamaterial (with $\varepsilon_{rz} = 1.3$ and $\varepsilon_{r\varphi}$ linearly varying from 1.5 to 2.2)[55]. Figure 3b shows the entire strip of unit cells along the radial direction, which consists of the linear-profile medium ($r_1 \leq r < r_2$) and the designed spatial Lorentz-profile medium ($r_2 \leq r < r_3$). The linear-profile medium is composed of 50 layers (each layer is 1 mm thick) along the radial direction, where the first 20 layers are the dielectric-air composite and the last 30 layers are the cut-wire metamaterial. The detailed design and geometric dimensions of the linear-profile medium is given in Supplementary Note 4.

Figure 3c plots the entire axial permittivity (left panel) and permeability (right panel) of this air-matched layered KK medium (gray region: $r_1 \leq r < r_3$), as a function of r at two different frequencies 10 GHz and 10.5 GHz. At both frequencies, the layered KK medium (1) supports spatial electric and magnetic Lorentz resonances simultaneously, and (2) is impedance matched to free space at $r = r_1$ for both TE and TM polarizations. In other words, the layered KK medium designed above is expected to achieve polarization-independent absorption over a bandwidth of at least 0.5 GHz from 10 to 10.5 GHz. To illustrate its absorption performance, we calculate the absorptance A with respect to the frequency and incident angle based on the retrieved parameters. The results given in Fig. 3d, e show that, in the frequency range from 9.8 to 11.0 GHz (9.7−10.9 GHz), the absorptance is over 99% for TE (TM) polarizations when the incident angle is less than 78° (74°). It is seen that the absorption of TE wave is better than that of TM wave, especially for large incident angles (around 75°− 85°). It comes from the different frequency dispersions of permittivity and permeability, as shown in Fig. 2b. The relative permittivity approaches to 1.2 at low frequencies while the relative permeability approaches to 1. The different asymptotic values of ε and μ at low frequencies originate from the non-magnetic substrate, of which $\varepsilon_s > 1$ and $\mu_s = 1$. As a result, the permeability of the designed KK medium experiences a sharper change at r_2 than the permittivity. Finite element simulations based on CST Microwave Studio have also been performed to analyze the absorption performance of the real structure. The results given in Supplementary Note 5 reveal an omnidirectional absorption over 90% from 9.95 to 11.01 GHz and 9.65 to 10.69 GHz for TE and TM polarizations, respectively.

To realize a miniaturized anechoic chamber, we roll up the layered KK medium (consisting of 5 cm thick linear-profile medium and 7.5 cm thick Lorentz-profile medium) into an annulus structure with an inner radius of 10 cm and an outer one of 22.5 cm. Full-wave simulations are performed while placing a line source inside the anechoic chamber. Figure 3f, g depict the results for TE and TM polarizations, respectively. In panels I and II, the line source is placed at $(0, 0)$ and $(9\,\text{cm}, 0)$ and the incident frequency is set to 10 GHz. Similar results under 10.5 GHz incidence are plotted in panels III and IV. As expected, neither TE nor TM incidence leads to observable standing wave or phase distortion, e.g., the maximum standing wave ratios R_{max}/R_{min} for panels (I)−(IV) in Fig. 3f, g are only 1.040 (1.012), 1.260 (1.122), 1.041 (1.052), and 1.294 (1.124), respectively. Similar to Fig. 1d, the incoming radiations at different frequencies are significantly dissipated around the corresponding spatial Lorentz resonances. The 1D plots of the fields along the x-axis given in Supplementary Note 6 show that the field

intensities are depleted by more than 60 dB and 90 dB within the KK medium for TE and TM polarizations, respectively. These results confirm that the layered KK medium can perform omnidirectional polarization-independent absorption, similar to the homogeneous one studied in Fig. 1.

Experimental measurements

To verify the polarization-independent absorption behavior, we perform the measurement of the field distributions within the fabricated anechoic chamber, as shown in Fig. 4a. Fabrication details can be found in the Methods section. For the TE polarization, a 2-dimensional (2D) omnidirectional monopole antenna is placed inside the anechoic chamber to serve as the source, whilst another monopole antenna is used as the probe to measure the local electric fields. The source and probe antennae are connected to the input and output ports of a network analyzer (Agilent E8361A), respectively. For the TM polarization, the monopole antennae are replaced by omnidirectional loop antenna and the local magnetic fields are measured using a similar procedure. Figures 4b and c plot the measured amplitude and phase (in the form of cos (phase)) distributions of the z-polarized electric fields under TE incidence. Corresponding results under TM incidence are shown in Fig. 4d, e. The measurements are performed at two frequencies, 10 GHz (panels I and II) and 10.5 GHz (panels III and IV), and for two source locations, $(0, 0)$ (panels I and III) and $(9\,\text{cm}, 0)$ (panels II and IV). Apparently, for all cases, the amplitude of the field varies smoothly and decreases slowly away from the source antenna without obvious reflection, with successfully compressed phase distortion.

We also assess quantitatively the quiet zone of the fabricated anechoic chamber by measuring the perturbation of S_{11}. Here, S_{11} denotes the reflection coefficient of the probe antenna, which was firstly calibrated by placing the antenna in free space (as a "matched load"). Thus, the probe antenna can work with the highest sensitivity to the adjacent scatterers. Then, we placed the probe inside the designed miniaturized anechoic chamber and measured S_{11} point by point. In such a case, $|S_{11}|$ distributions can be used to evaluate the reflection from the anechoic chamber. The smaller the $|S_{11}|$, the better the anechoic chamber. Detailed measurement process and experimental results are presented in Supplementary Note 7. Supplementary Fig. 6 demonstrates that the perturbed $|S_{11}|$ (dB) is less than −29 dB and −33 dB for TE and TM polarization, respectively, a clear proof that the miniaturized anechoic chamber designed with the KK medium is an artificial analogue of free space for both TE and TM polarizations. We highlight that the tiny fluctuations of the measured S_{11} result from the discontinuous edges of the KK medium along the z-direction, which can be further suppressed by increasing the height of the sample.

Conclusions

In conclusion, a polarization-independent KK medium is experimentally realized in this work. The key to our design is a special matryoshka metamaterial that can support both magnetic and electrical resonances at the same frequency with negligible crosstalk. This design not only provides a feasible solution to the longstanding problem, i.e., to achieve broadband, omnidirectionally matched absorption of unpolarized wave, but also adds a new perspective on the metamaterial design to overcome the polarization limitation. An annulus-shaped anechoic chamber with a diameter of 6.83 wavelengths was fabricated. It can achieve omnidirectional polarization-independent absorption for both TE and TM polarizations, as confirmed by both numerical simulations and experimental measurements.

Considering that the designed spatial resonance positions get farther away from the inner truncation boundary as the frequency decreases, as shown in Fig. 3c, the operating frequencies can be further extended to lower ones only if we add more gradient units along the r direction to cover the resonance regions. In such a case, the operating bandwidth can be flexibly controlled by tuning the outer truncation positions of the space-frequency KK medium. Meanwhile, it should be noted that the designed KK medium is actually only for 2D case, due to the anisotropic building units. If the resonant units are deliberately designed to be 3D isotropic, the proposed
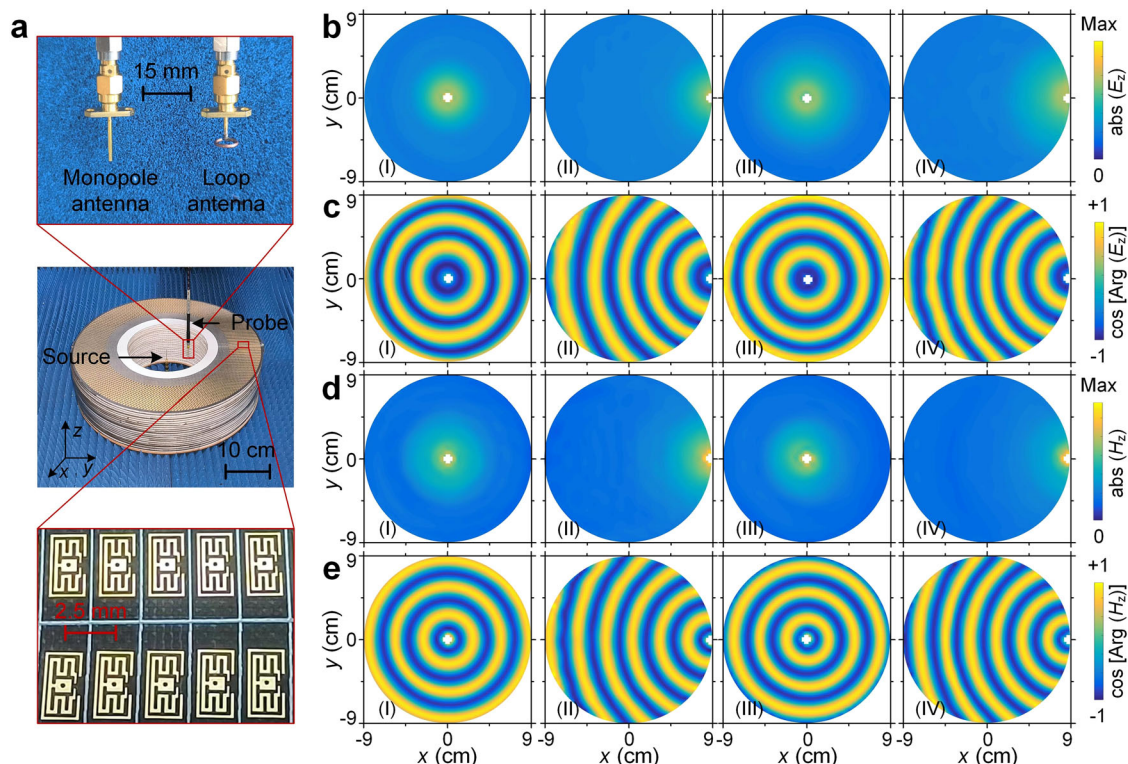
Fig. 4 | Experimental setup and measured results. a Photograph of the fabricated sample and experimental setup. Top two insets show the antennae exciting and receiving TE, and TM waves, respectively. **b, c** Measured amplitude (**b**) and phase (**c**) distributions of the z-polarized electric field in the air region, respectively, where the phase distributions are plotted in the form of cos (phase). Panels I and II show the results measured at 10 GHz when the line source is located at (0, 0), and (9 cm, 0), respectively. Panels III, IV show the corresponding results at 10.5 GHz for two source locations. **d, e** Corresponding measured amplitude (**d**) and phase (**e**) distributions of the z-polarized magnetic field.

approach can also be easily extended to the full 3D case, such as designing all-dielectric spherical or cubic resonators[56]. Certainly, they can also be designed using 3D symmetrical metallic structures but with more complicated shapes[57]. Finally, this method can also be extended to higher frequencies such as near-infrared and optical regimes, using all-dielectric Mie resonators instead of metallic structures, which have been widely used to construct optical metamaterials[56,58]. This approach provides a new route to realize ideal absorbers, and shows great application prospect in stealth technology, electromagnetic compatibility, and photodetection.

Methods
In the practical implementation, we fabricate the layered KK medium using PCB printing. Figure 4a depicts the fabricated annulus-shaped KK medium, with all geometric dimensions the same as those in Fig. 3f, g. Microwave-transparent foam plates with a thickness of 4.8 mm are placed between each PCB layer along the z-axis to support the sample. A total of 20-layer PCB samples are stacked in the z-direction. Finally, the miniaturized anechoic chamber with a 10 cm inner radius, 22.5 cm outer radius, and 12 cm height is obtained.

Data availability
All data supporting the findings of this study are present in the paper and the Supplementary information. Additional data related to this paper can be requested from the corresponding authors.

Code availability
Relevant codes are available from the corresponding authors upon reasonable request.

References
1. Qu, S., Hou, Y. & Sheng, P. Conceptual-based design of an ultrabroadband microwave metamaterial absorber. *Proc. Natl Acad. Sci. USA* **118**, e2110490118 (2021).
2. Han, T. C., Wen, K. H., Xie, Z. X. & Yue, X. L. An ultra-thin wideband reflection reduction metasurface based on polarization conversion. *Prog. Electromagn. Res.* **173**, 1–8 (2022).
3. Tsakmakidis, K. L., Boardman, A. D. & Hess, O. Can light be stopped in realistic metamaterials? Reply. *Nature* **455**, E11–E12 (2008).
4. Jiménez, N., Romero-García, V., Pagneux, V. & Groby, J.-P. Rainbow-trapping absorbers: broadband, perfect and asymmetric sound absorption by subwavelength panels for transmission problems. *Sci. Rep.* **7**, 13595 (2017).
5. H. W. Ott. *Electromagnetic compatibility engineering*. (John Wiley & Sons, Hoboken, NJ, USA, 2011).
6. Li, D. D. et al. Highly transparent tunable microwave perfect absorption for broadband microwave shielding. *Prog. Electromagn. Res.* **176**, 35–44 (2023).
7. D. M. Pozar. *Microwave engineering*. (John Wiley & Sons, Hoboken, NJ, USA, 2011).
8. Khan, H. A. et al. Transparent conformal metasurface absorber for ultrawideband radar cross section reduction. *J. Phys. D. Appl. Phys.* **57**, 135105 (2024).
9. Raman, A. P., Anoma, M. A., Zhu, L., Rephaeli, E. & Fan, S. Passive radiative cooling below ambient air temperature under direct sunlight. *Nature* **515**, 540–544 (2014).
10. L. H. Hemming. *Electromagnetic anechoic chambers*: a fundamental design and specification guide. (Wiley, Hoboken, NJ, USA, 2002).
11. Togawa, H., Hatakeyama, K. & Yamauchi, K. Reflectivity measurements in anechoic chambers in the microwave to millimeter range. *IEEE Trans. Electromagn. Compat.* **47**, 312–319 (2005).

12. Cai, Z. et al. Small anechoic chamber design method for on-line and on-site passive intermodulation measurement. *IEEE Trans. Instrum. Meas.* **69**, 3377–3387 (2020).

13. Expósito, I., Sánchez, M. G. & Cuiñas, I. Uncertainty assessment of a small rectangular anechoic chamber: from design to operation. *IEEE Trans. Antennas Propag.* **68**, 4871–4880 (2020).

14. Landy, N. I., Sajuyigbe, S., Mock, J. J., Smith, D. R. & Padilla, W. J. Perfect metamaterial absorber. *Phys. Rev. Lett.* **100**, 207402 (2008).

15. Huang, X. T., Lu, C. H., Rong, C. C., Wang, S. M. & Liu, M. H. Wide angle of incidence-insensitive polarization-independent THz metamaterial absorber for both TE and TM mode based on plasmon hybridizations. *Materials* **11**, 671 (2018).

16. Wang, B. et al. Theoretical investigation of broadband and wide-angle Terahertz metamaterial absorber. *IEEE Photonics Technol. Lett.* **26**, 111–114 (2014).

17. Cheng, Y., Gong, R. & Cheng, Z. A photoexcited broadband switchable metamaterial absorber with polarization-insensitive and wide-angle absorption for terahertz waves. *Opt. Commun.* **361**, 41–46 (2016).

18. Wang, B. Quad-band Terahertz metamaterial absorber based on the combining of the dipole and quadrupole resonances of two SRRs. *IEEE J. Sel. Top. Quantum Electron.* **23**, 1–7 (2017).

19. Riley, C. T. et al. Near-perfect broadband absorption from hyperbolic metamaterial nanoparticles. *Proc. Natl Acad. Sci. USA* **114**, 1264–1268 (2017).

20. Cui, Y. et al. Ultrabroadband light absorption by a sawtooth anisotropic metamaterial slab. *Nano Lett.* **12**, 1443–1447 (2012).

21. Peng, T. et al. Miniaturized anechoic chamber constructed based on an inhomogeneous PML model. *IEEE Trans. Microw. Theory Tech.* **67**, 3595–3602 (2019).

22. Peng, T. et al. A compact microwave imager integrated with a miniaturized dual-angle anechoic chamber. *IEEE Trans. Microw. Theory Tech.* **69**, 4831–4839 (2021).

23. Ye, D. et al. Towards experimental perfectly-matched layers with ultra-thin metamaterial surfaces. *IEEE Trans. Antennas Propag.* **60**, 5164–5172 (2012).

24. Berenger, J.-P. A perfectly matched layer for the absorption of electromagnetic waves. *J. Comput. Phys.* **114**, 185–200 (1994).

25. Sacks, Z. S., Kingsland, D. M., Lee, R. & Jin-Fa, L. A perfectly matched anisotropic absorber for use as an absorbing boundary condition. *IEEE Trans. Antennas Propag.* **43**, 1460–1463 (1995).

26. Ye, D. et al. Ultrawideband dispersion control of a metamaterial surface for perfectly-matched-layer-like absorption. *Phys. Rev. Lett.* **111**, 187402 (2013).

27. Kottos, T. Broken symmetry makes light work. *Nat. Phys.* **6**, 166–167 (2010).

28. Lin, Z. et al. Unidirectional invisibility induced by PT-symmetric periodic structures. *Phys. Rev. Lett.* **106**, 213901 (2011).

29. Castaldi, G., Savoia, S., Galdi, V., Alù, A. & Engheta, N. PT metamaterials via complex-coordinate transformation optics. *Phys. Rev. Lett.* **110**, 173901 (2013).

30. Leonhardt, U. Optical conformal mapping. *Science* **312**, 1777–1780 (2006).

31. Pendry, J. B., Schurig, D. & Smith, D. R. Controlling electromagnetic fields. *Science* **312**, 1780–1782 (2006).

32. Horsley, S. A. R., Artoni, M. & La Rocca, G. C. Spatial Kramers–Kronig relations and the reflection of waves. *Nat. Photonics* **9**, 436–439 (2015).

33. Horsley, S. A. R., Artoni, M. & La Rocca, G. C. Reflection of waves from slowly decaying complex permittivity profiles. *Phys. Rev. A.* **94**, 063810 (2016).

34. Horsley, S. A. R. & Longhi, S. One-way invisibility in isotropic dielectric optical media. *Am. J. Phys.* **85**, 439–446 (2017).

35. Horsley, S. A. R. & Longhi, S. Spatiotemporal deformations of reflectionless potentials. *Phys. Rev. A.* **96**, 023841 (2017).

36. King, C. G., Horsley, S. A. R. & Philbin, T. G. Zero reflection and transmission in graded index media. *J. Opt.* **19**, 085603 (2017).

37. Longhi, S., Horsley, S. A. R. & Della Valle, G. Scattering of accelerated wave packets. *Phys. Rev. A.* **97**, 032122 (2018).

38. Loran, F. & Mostafazadeh, A. Broadband directional invisibility. *Appl. Phys. Lett.* **123**, 191104 (2023).

39. Lee, K., Lim, J. & Park, Y. Full-field quantitative X-ray phase nanotomography via space-domain Kramers–Kronig relations. *Optica* **10**, 407–414 (2023).

40. Wang, Y.-X., Zhang, Y., Du, L. & Wu, J.-H. Chiral phase modulation and a tunable broadband perfect absorber using a coherent cold atomic ensemble. *Phys. Rev. A.* **108**, 053716 (2023).

41. Jiang, W. et al. Deformable broadband metamaterial absorbers engineered with an analytical spatial Kramers-Kronig permittivity profile. *Laser Photonics Rev.* **11**, 1600253 (2017).

42. Ye, D. et al. Observation of reflectionless absorption due to spatial Kramers–Kronig profile. *Nat. Commun.* **8**, 51 (2017).

43. Li, Q. et al. A miniaturized anechoic chamber: omnidirectional impedance matching based on truncated spatial Kramers–Kronig medium. *Adv. Opt. Mater.* **10**, 2200381 (2022).

44. Aydin, K., Ferry, V. E., Briggs, R. M. & Atwater, H. A. Broadband polarization-independent resonant light absorption using ultrathin plasmonic super absorbers. *Nat. Commun.* **2**, 517 (2011).

45. Yu, P. et al. Broadband metamaterial absorbers. *Adv. Opt. Mater.* **7**, 1800995 (2019).

46. Ding, F., Cui, Y., Ge, X., Jin, Y. & He, S. Ultra-broadband microwave metamaterial absorber. *Appl. Phys. Lett.* **100**, 103506 (2012).

47. Liu, D. et al. Designing spatial Kramers–Kronig media using transformation optics. *IEEE Trans. Antennas Propag.* **68**, 2945–2949 (2020).

48. Bergman, D. J. The dielectric constant of a composite material-A problem in classical physics. *Phys. Rep.* **43**, 377–407 (1978).

49. Gao, Y. et al. Tunable broadband angular selectivity for s-polarized terahertz incidences. *Appl. Phys. A Mater. Sci. Process.* **127**, 127 (2021).

50. Ye, D., Chang, K., Ran, L. & Xin, H. Microwave gain medium with negative refractive index. *Nat. Commun.* **5**, 5841 (2014).

51. Ye, D., Li, B., Zhu, Z., Yang, Y. & Wang, Z. Achieving volumetric gain metamaterials. *AIP Adv.* **9**, 055314 (2019).

52. Li, H. et al. Dual-band fresnel zone plate antenna with independently steerable beams. *IEEE Trans. Antennas Propag.* **66**, 2113–2118 (2018).

53. Li, H. et al. Reconfigurable diffractive antenna based on switchable electrically induced transparency. *IEEE Trans. Microw. Theory Tech.* **63**, 925–936 (2015).

54. Chen, X., Grzegorczyk, T. M., Wu, B.-I., Pacheco, J. & Kong, J. A. Robust method to retrieve the constitutive effective parameters of metamaterials. *Phys. Rev. E.* **70**, 016608 (2004).

55. Pendry, J. B., Holden, A. J., Stewart, W. J. & Youngs, I. Extremely low frequency plasmons in metallic mesostructures. *Phys. Rev. Lett.* **76**, 4773–4776 (1996).

56. Jahani, S. & Jacob, Z. All-dielectric metamaterials. *Nat. Nanotechnol.* **11**, 23–36 (2016).

57. Wang, C. et al. Nearly ideal transparency with artificially designed meta-atoms. *Adv. Mater.* **36**, 2308298 (2024).

58. Vynck, K. et al. All-dielectric rod-type metamaterials at optical frequencies. *Phys. Rev. Lett.* **102**, 133901 (2009).

Acknowledgements

Author contributions

Q.L., Y.L., D.Y. designed the research; Q.L., Y.L., J.Z., Y.G., J.T., X.H., D.Y. performed the research. All authors contributed to data interpretation and the composition of the manuscript.

Competing interests

The authors declare no competing interests.

Additional information

Supplementary information The online version contains supplementary material available at https://doi.org/10.1038/s42005-024-01639-0.

Correspondence and requests for materials should be addressed to Yu Luo, Jingjing Zhang or Dexin Ye.

Peer review information *Communications Physics* thanks the anonymous reviewers for their contribution to the peer review of this work. A peer review file is available.

Reprints and permissions information is available at http://www.nature.com/reprints